

Revision 1

Word Count: 7405

Hydration-driven stabilization and volume collapse of grain boundaries in Mg_2SiO_4 forsterite predicted by first-principles simulations

Dipta B. Ghosh^{1,2}, Bijaya B. Karki^{1,2,3}, and Jianwei Wang^{2,3}

¹School of Electrical Engineering and Computer Science, ²Department of Geology and Geophysics,

³Center for Computation and Technology

Louisiana State University, Baton Rouge, LA 70803, USA

ABSTRACT

Grain boundaries in mantle minerals are of critical importance to geophysical and geochemical processes of the Earth's interior. One of the fundamental issues is to understand how the water (H_2O) component influences the properties of grain boundaries in silicate materials. Here, we report the results of the structure and stability of several tilt grain boundaries in Mg_2SiO_4 forsterite over the pressure range 0 to 15 GPa using density functional theory-based first-principles simulations. The results suggest greater energetic stability and hydration-driven volume collapse (negative excess volume) at zero pressure for the majority of hydrous grain boundaries relative to the anhydrous (dry) ones. All the hydrous grain boundaries become increasingly favorable at elevated pressures as the calculated hydration enthalpy systematically decreases with the increasing pressure. The hydrous components at the interfacial regions are predominantly in the hydroxyl form and to a lesser extent in the molecular H_2O form. Their calculated ratio ranges from 1.6 to 8.7 among the different grain boundary configurations. Our structural analysis also reveals that the hydroxyls are bound to either both Mg and Si or to Mg only. In comparison, the molecular species are bound only to Mg sites. Besides direct oxygen-hydrogen bonding, intermolecular hydrogen bonding becomes important with

compression. On the basis of our results, we suggest that local atomic rearrangements caused by dissociative adsorption of water facilitates efficient compaction of the boundary interfaces which, in turn, results in greater relative stability of hydrous grain boundaries. This means that water prefer to be incorporated within the grain boundaries over the bulk of silicate materials.

INTRODUCTION

Defects that are usually present in materials in various forms influence the properties of materials to various degrees. In particular, the inter-granular regions or interfaces (i.e., grain boundaries) can act as sinks for other defects, including impurities (Hiraga et al., 2003, 2004; Karki et al., 2015). They may act as nucleation sites for corrosion, precipitation, fracture and affect plastic deformation properties of materials (Duffy, 1986; Sutton and Balluffi, 1995; Yang et al., 2015; Barr et al., 2018). Additionally, they are known to provide faster pathways for ionic diffusion and electrical conduction (Van Orman et al., 2003; Hayden and Watson, 2007, 2008; Dohmen, 2008; Pommier et al., 2018). The behavior and properties of grain boundaries in ceramics and minerals are of critical importance from technological and geological viewpoints.

Water, a universal solvent, can have profound influence on various materials properties, including creep, elasticity, and melting (Hirth and Kohlstedt, 1995; Henderson, 2002; Asimow and Langmuir, 2003; Carrier et al., 2016; Suknev, 2019). The presence of hydrous components at grain boundary interfaces is likely to amplify the transport properties, such as diffusion, and electrical conductivity and influence seismic wave velocities (Karato, 1990; Karato and Wu, 1993). This is especially relevant for materials in subduction zones and upper mantle-transition regions where the presence of water is expected in significant amounts.

Here we choose to study hydrous grain boundaries in forsterite (Mg_2SiO_4) which is the Mg end-

member of the olivine system and is a common rock-forming mineral in Earth's upper mantle. Forsterite in its hydrated form has widely been studied (e.g., Kohn 1996; Jacobsen et al., 2008; Ye et al., 2009; Liu et al., 2018). Forsterite–water interactions are thought to be one of the key processes behind water retention during planetary accretion (Stimpfl et al., 2006; King et al., 2010). The presence of hydrous components is also considered to promote incipient melting and enhance interfacial transport at mantle conditions (Hirth and Kohlstedt, 1995; Henderson, 2002; Asimow and Langmuir, 2003). In the study of nominally anhydrous forsterite, both OH and molecular water species were predicted to exist, with the possibility of clustered OH resembling to static H₂O at grain boundary interfaces and non-clustered OH units as bulk point defects (Kohn, 1996). Associating the hydrous components with forsterite grain boundaries is thus important with regard to mantle materials.

Investigating how H₂O interacts with the grain boundary and what characteristic changes occur at the atomic scale can assist us to understand the fundamental processes that occur in grain boundaries under pressure and wet conditions. Due to the lack of atomic order at the grain boundary, the widely used two-dimensional experimental imaging techniques (e.g., transmission electron microscopy, electron back-scattered diffraction) often fall short in fully resolving the three-dimensional structure of the interfaces (Marquardt and Faul, 2018). The presence of hydrous component is expected to further complicate experimental characterizations of the interfaces. An accurate determination of the speciation of the hydrous component by vibrational techniques remains a great challenge under pressure, although such effort has been made at ambient conditions (Geisler et al., 2019). Our first-principles computational approach is expected to be particularly helpful in this regard. Previous computational studies have investigated grain boundaries in forsterite (de Leeuw et al., 2000a; Adjaoud et al., 2012) and proton-containing defects at tilt grain boundaries using interatomic interaction potentials (de Leeuw et al., 2000a) at 0 GPa. Proton-free grain boundaries in forsterite were previously studied using the first-principles method in the pressure range 0 – 17 GPa (Ghosh and Karki, 2014).

In this work, we use first-principles computations to evaluate the properties of hydrous grain boundaries of $(011)/[100]$ and $(110)/[001]$ types for the pressure range 0 – 15 GPa. Specifically, local structure, bond distance, formation enthalpy, and excess volume of hydrated grain boundaries were calculated. The results allow us to evaluate the relative stability and excess properties in comparison to dry grain boundaries, considering different tilt angles for each grain boundary type. They also allow us to identify the interfacial speciation of the hydrous component and perhaps answer the fundamental question of whether hydrogen is fractionating to grain boundaries.

GRAIN BOUNDARY MODELS AND COMPUTATIONAL DETAILS

For each of the grain boundary systems studied here, the computational model is a bicrystal which comprises of two oppositely oriented blocks (one block being the mirror image of the other block) of the crystal merged at the interface (Verma and Karki, 2010; Ghosh and Karki, 2014). This results in a grain boundary interface at the center of the bi-crystal supercell. The imposed periodic boundary conditions introduce another oppositely oriented grain boundary split across the supercell edges (Fig. 1). To minimize interactions between two grain boundaries the supercells were constructed in a rectangular shape with inter-granular distance (i.e., the width of crystal block) of larger than 15 Å.

We consider two types of tilt boundaries, $(011)/[100]$ and $(110)/[001]$, which are common in forsterite and have been previously studied (Leeuw et al., 2000a; Ghosh and Karki, 2014). In the $(011)/[100]$ type, a is the axis of rotation and the grain boundary plane is perpendicular to the c axis (Fig. 1). In the $(110)/[001]$ type, c is the rotation axis and the grain boundary plane is perpendicular to the b axis. To account for low and high angle grain boundaries, three different tilt angles spanning over an angular range of 30° were considered for each grain boundary type (Fig. 1 and Table I). To create a wet grain boundary, both cations (Mg and Si) in the interfacial region were substituted in proportion with an appropriate number of hydrogen atoms (2 for Mg and 4 for Si) so that the stoichiometry of Mg_2SiO_4 remains

unchanged and the system maintains charge neutrality as well. This system effectively represents the result of the interaction of water (H_2O) with dry grain boundary expressed as $n\text{Mg}_2\text{SiO}_4 + 4x\text{H}_2\text{O} \rightarrow \text{Mg}_{2n}\text{Si}_n\text{O}_{4(n+x)}\text{H}_{8x}$, where n is the number of formula units of Mg_2SiO_4 in dry boundary and x is the number of H_2O units incorporated in the grain boundary. The addition of 8 hydrogen atoms for every three cation substitutions (2 Mg and 1 Si corresponding to one Mg_2SiO_4 unit) results in a higher atomic population at the interface relative to the bulk. Special attention was given during modeling and simulation to correct any possible artifacts, including that of two hydrogen atoms coming too close ($\sim 1.2 \text{ \AA}$) to form molecular hydrogen (H_2).

Both the planar and stepped grain boundary configurations were modeled for the (011)/[100] type whereas only the stepped configurations were modeled for (110)/[001]. Due to the step-like structure in the interface, the stepped dry grain boundaries generally possess larger excess volumes (or lower interfacial atomic density) and are less stable than their planar counterparts (Ghosh and Karki, 2014). The present study aims at exploring the effects of large excess volumes on the stability of the grain boundaries at hydrated conditions.

First-principles simulations were performed using the generalized gradient approximation (GGA) to the density functional theory (Perdew et al., 1996) and the projector augmented wave method (Kresse and Joubert 1999) as implemented in VASP (Kresse and Furthmuller 1996). Plane wave basis set with an energy cut-off of 900 eV, Gamma point Brillouin zone sampling, force threshold of 0.01 eV/Å, and an energy convergence criterion of 10^{-6} eV were used. Depending on the grain boundary type and hydrous content, the number of atoms in the simulation supercells varies between 412 and 900 (Table I). The use of larger supercells was shown to have insignificant effects on atomic arrangements near the boundaries and the energy of the grain boundaries (Ghosh and Karki, 2014). In the present work, similar supercell sizes were adopted as in our previous work (Ghosh and Karki, 2014). Static simulations

(corresponding to 0 K) were performed at different volumes to capture the effects of pressure over the range 0 to ~15 GPa. The rationale behind using GGA in this study is that the properties of water are constrained more accurately with this approximation compared to LDA (local density approximation) (Gillan et al., 2016). To assess the differences due to the choice of exchange-correlation functionals, additional simulations were performed for dry and hydrous planar 30.4° and 49.6° tilt grain boundaries using LDA as in the previous study (Ghosh and Karki, 2014).

The formation enthalpy of dry grain boundary is evaluated as:

$$\Delta H_{GB} = 0.5(H_{GB} - H_B)/A_{GB} \quad (1)$$

where H_{GB} is the enthalpy of the simulated grain boundary system, H_B is the enthalpy of the corresponding perfect bulk super-cell (that contains the same number of Mg_2SiO_4 units as the grain boundary system), and A_{GB} is the area of one grain boundary interface. The factor 0.5 accounts for two oppositely oriented grain boundaries contained in the supercell (Fig. 1).

To evaluate the formation enthalpy of wet (hydrous) grain boundary, the enthalpy of water component has also to be accounted for by using:

$$\Delta H_{hyGB} = 0.5(H_{hyGB} - H_B - H_{H_2O})/A_{GB} \quad (2)$$

where H_{hyGB} , H_{H_2O} represent the enthalpy of hydrous grain boundary system and water component, respectively. We simulated bulk water in its amorphous phase (that is, frozen liquid water) at 0 K at different volumes to evaluate ΔH_{hyGB} . Because only relative energies are considered, any inadequacies that may arise due to insufficient Brillouin zone sampling, choice of the exchange-correlation functional, supercell size, etc. are largely canceled out in evaluating the energy differences between the systems.

The excess volume for the dry grain boundary can be evaluated as:

$$\Delta V_{GB} = 0.5(V_{GB} - V_B)/A_{GB} \quad (3)$$

where V_{GB} and V_B represent the volume of the dry grain boundary system and the perfect crystal for the same number of Mg_2SiO_4 units, respectively.

Similarly, for wet grain boundaries, the excess volume can be evaluated as:

$$\Delta V_{hyGB} = 0.5(V_{hyGB} - V_B - V_{H_2O})/A_{GB} \quad (4)$$

where V_{hyGB} , V_B , and V_{H_2O} represent the volume of the hydrous grain boundary system, the perfect crystal, and the water component, respectively.

RESULTS AND DISCUSSION

Grain boundary structure and energetics

As shown in Fig 2 (and Fig. S1, S2), the structure remains same in the bulk regions of dry and wet grain boundaries. The hydrous component is efficiently incorporated at the interface resulting in a higher number density of atoms in the interfacial region (note that 8 hydrogen atoms are substituted for 2 Mg and 1 Si atoms). Modeled anhydrous and hydrous grain boundary systems before relaxation for the 30.4° planar and stepped configurations are shown in Fig. 2a and 2b. Hydrogen atoms were kept at distances $\geq 1.5 \text{ \AA}$ for H-Mg and H-Si, $\geq 1.2 \text{ \AA}$ for H-O, and $\geq 1.0 \text{ \AA}$ for H-H. This somewhat reduces the possible bonding bias of hydrogen that arises from modeling. It is clear from relaxed hydrous grain boundary at 0 GPa (Fig. 2c) that all hydrogen atoms are bonded with oxygen atoms. Both OH and H_2O species are clearly visible with a predominance of hydroxyls. There is no noticeable change in the hydrogen speciation with compression (Fig. 2c and 2d). However, pressure-induced spatial rearrangements (such as bond rotations, decrease in bond distances) result in increased compaction of the grain boundary region.

Analysis of local surroundings of Mg and Si in the bulk and boundary regions can provide insight into structural variations at the atomic level. Both Mg and Si cations remain under polyhedral surroundings

in Mg_2SiO_4 . Polyhedral distortion index defined as $\delta_\lambda = \frac{1}{n} \sum_1^n \frac{\lambda_i - \lambda_{av}}{\lambda_{av}}$, where λ_i and λ_{av} are the individual and average bond lengths, respectively, is a good indicator of structural characteristics. For the bulk regions (away from the interface), both the average bond length and polyhedral distortion index almost overlap with the corresponding values of the pure crystal (Fig. 3). For the interfacial regions, both structural parameters show large deviations from their corresponding crystalline values (Fig. 3). Distortion index reaches as high as 6% for the octahedral Mg sites with longer Mg-O bonds (note that there are two distinct Mg crystalline sites in forsterite with different average Mg-O bond lengths, see right panel Fig. 3). The distortion index value for individual Si-O polyhedron remains within 3%. Considering all grain boundary systems simulated at 0 GPa, the average distortion index (which is averaged over all Mg for any specific configuration) for Mg varies from 2.3 – 2.7%. For Si, this range is 0.9 – 1.15%. The Si distortion value displays an increasing trend with compression. On the contrary, the Mg distortion value tends to decrease with increasing pressure (Fig. 3). The average distortion index for Si in dry grain boundaries remains lower than that of the corresponding hydrous grain boundary values at all pressures. For Mg, the hydrous cases display a lower average distortion index than their dry counterparts for the majority of the grain boundaries.

The grain boundary formation enthalpy varies considerably among different configurations for both dry and wet grain boundaries as shown in Fig 4. At zero pressure, the calculated enthalpy varies between 0.65 and 1.8 J/m² for the tilt angle range 30.4° – 65.0° without showing any clear trend (Fig. S3). For instance, dry grain boundaries display the lowest enthalpy for the 49.6° tilt whereas hydrous grain boundaries show increasing enthalpy with the tilt angle. For the smallest tilt angle 30.4°, hydrous grain boundaries have significantly lower formation enthalpies than their dry counterparts for both planar and stepped configurations. The opposite trend can be seen for the highest tilt angle 60.4°. It is likely that hydration-driven stabilization of grain boundaries depends significantly on specific boundary

configuration and tilt angle. However, our finding that the grain boundary formation energies fall within a narrow range of about 1.0 J/m^2 at zero pressure indicates the possible existence of different types of grain boundaries in real systems. Our predicted energetics is consistent with the previous computational findings for dry grain boundary based on interaction potentials (Leeuw et al., 2000a; Adjaoud et al., 2012) and the first-principles approach (Ghosh and Karki, 2014).

The formation enthalpy of all dry grain boundaries with planar and stepped configurations increases monotonically with increasing pressure (Fig. 4) as also predicted previously (Ghosh and Karki, 2014). The extent of the pressure-induced variation in the formation enthalpy, however, differs considerably among different grain boundaries. The variations are small ($\sim 0.5 \text{ J/m}^2$) for the 30.4° and 49.6° tilts, but they are as large as $\sim 2.0 \text{ J/m}^2$ for the 60.4° tilt when both planar and stepped configurations of the (011)/[100] type are considered. Among all dry grain boundary systems simulated, the planar 49.6° tilt remains energetically most favorable at all pressures.

Interestingly, the formation enthalpy of hydrous grain boundaries shows modest variations with pressure (Fig 4). Considering all hydrous grain boundaries, the pressure-induced changes in the enthalpy over the range 0 – 15 GPa remains within 0.5 J/m^2 . In contrast, this variation is as high as 2 J/m^2 for dry cases. In particular, the formation enthalpy for hydrous 30.4° and 49.6° tilts show a weak non-monotonic trend with pressure and varies by less than 0.25 J/m^2 over the pressure range considered. The 30.4° and 49.6° tilt grain boundaries remain energetically competitive at all pressures and have much smaller formation enthalpy than that of the 60.4° tilt grain boundaries. Moreover, hydrous grain boundaries have higher formation enthalpy than their dry counterparts at zero pressure but they become more favorable above 3 GPa. Unlike the (011)/[100] type, the formation enthalpy of hydrous stepped (110)/[001] grain boundaries, irrespective of tilt angle, remains relatively high at all pressures. It is worth noting that the LDA calculations for selected (30.4° and 49.6° tilt) dry and

hydrous grain boundaries display comparable values and similar pressure effects to the GGA calculations. On the basis of our first-principles results, it is thus clear that hydrous grain boundaries consistently have lower formation enthalpies than their dry counterparts at elevated pressures. In particular, the (011)/[100] type hydrated boundaries are likely to be prevalent at compressed conditions because of their low formation enthalpy (Fig. 4).

Excess volume at the grain boundary

The average density of atoms at the interfaces is expected to be low compared to the bulk crystal due to distorted arrangement in grain boundaries. This may render grain boundary systems to retain finite (positive) excess volume as shown by a number of studies (Kuru et al., 2009; Verma and Karki, 2010; Adjaoud et al., 2012; Ghosh and Karki, 2014). Our results show that at zero pressure, dry grain boundaries have positive excess volume for all tilt angles (Fig. 5), consistent with the previous computational prediction (Ghosh and Karki, 2014). In contrast, the majority of the hydrous grain boundary systems simulated here (with the exception of stepped 60.4°) display negative excess volume at zero pressure (Fig. 5). This means that there is a volume collapse when hydrous components are introduced at the interfacial regions. A positive correlation between the grain boundary formation enthalpy and excess volume can be seen among all hydrous (011)/[100] grain boundaries. For instance, the formation enthalpy of hydrous stepped (011)/[100] boundaries at zero pressure increases from 0.65 to 1.55 J/m² as the tilt angle increases from 30.4° to 60.4° (Fig. 4b). For the same tilt angle range, the excess volume increases from -0.4×10^{-10} to 0.14×10^{-10} m³/m² (Fig. 5b). A similar trend can also be seen for hydrous planar (011)/[100] grain boundaries. The LDA results for excess volume are slightly smaller than the corresponding GGA results at all pressures.

The effects of pressure on the excess volume of hydrous grain boundaries are significantly different

when compared with the dry ones, especially at the initial stages of compression (Fig. 5). All dry grain boundaries display a nearly linear decrease in excess volume with compression and show larger excess volume than their hydrous counterparts. On the contrary, excess volume in hydrous grain boundaries shows a non-monotonic variation with pressure. For energetically most favorable (planar and stepped) 30.4° and 49.6° tilt grain boundaries of (011)/[100] type, large negative volumes can be seen at zero pressure. As pressure increases, the excess volume becomes less negative, remaining close to zero ($\pm 0.1 \times 10^{-10} \text{ m}^3/\text{m}^2$) over much of the pressure range studied. Other hydrous grain boundaries display positive excess volume at all pressures. Irrespective of the grain boundary type and tilt angle, the excess volumes in all hydrous grain boundaries remain smaller than their dry counterparts. The excess volume results from our LDA calculations are qualitatively comparable to the corresponding GGA values (Fig. 5a).

Speciation of hydrous component at the grain boundary

To understand how the hydrous component is incorporated at the grain boundary interfaces, we analyze its local structure and speciation. At zero pressure, our analysis reveals that hydroxyls (OH) and molecular water (H₂O) are present in significant amounts (Table I). The relative proportion of the two species varies among different grain boundaries, but a greater abundance of the hydroxyl species is apparent in all cases. At zero pressure, the OH:H₂O ratio displays a broad range of 1.6 – 8.7 when all grain boundaries are considered (Table I). The ratio for any given grain boundary shows some changes with compression but there is no clear trend and the ratio in several of them actually remains unchanged. We note here that temperature makes hydrogen atoms relatively more mobile and can change the speciation ratio. However, it is likely that hydroxyl still remains the dominant species at elevated temperatures. Our speciation results are generally consistent with the experimental observations of hydroxyls and clustered OH resembling static H₂O at grain boundary in nominally

anhydrous forsterite (Kohn, 1996).

The interfacial area and the number of interfacial cationic sites increase as the tilt angle increases. This means that the hydrogen number density ($\rho_H = 2x/A_{GB}$) at the interface varies among different grain boundary configurations. Considering all configurations, ρ_H varies from 0.15 to 0.28 per unit surface area of the interface at zero pressure and somewhat increases with pressure (Table I). The varying OH:H₂O ratio among different grain boundary configurations do not show any discernible trend with the hydrogen number density nor does it with tilt angle or interfacial configuration. It is possible that the availability of the reactive sites at the grain boundaries plays a more deterministic role in controlling the OH:H₂O ratio.

At the grain boundaries, the O-H species shares its oxygen atoms with cations, that is, the oxygen is also bonded to either Mg and Si both or Mg only. The ratio of H-O-Mg to H-O-Si connections for hydroxyls remains around 2:1 for all configurations at all pressures, consistent with the fact that for every Si there are two Mg atoms in the system. However, the H₂O species are exclusively adsorbed to Mg atoms. This exclusivity is present in all cases at all pressures. Depending on the grain boundary type, 50–80% of the oxygen atoms at the grain boundary regions remain undercoordinated with respect to cations (Mg, Si, and H) at zero pressure (Table I). These undercoordinated oxygen atoms are typically in a 3-fold state, compared to the bulk coordination number of 4 in Mg₂SiO₄. There is an increase in oxygen-cation connectivity with compression, but undercoordination persists at elevated pressures (Table I). Our analysis shows that except for a few five oxygen coordinated Si atoms in some grain boundaries (< 3% at 0 GPa), the majority of the interfacial Si atoms remain under tetrahedral coordination (Table I). The interfacial Si tetrahedra are noticeably distorted in comparison to their bulk tetrahedral arrangements. On the other hand, 4 – 21% interfacial Mg atoms are undercoordinated with oxygen at zero pressure (Table I) as compared to the octahedral coordination in the bulk. These

undercoordinated states are predominantly 5-fold and some 4-fold (up to ~5% at 0 GPa). The dominance of Mg involved coordination defect states suggests that reactive sites within grain boundaries are more likely to be associated with Mg's than the Si's. These undercoordinated cation species (which represent incomplete coordination) within grain boundaries may serve as reactive sites for the transport of reactive species, such as protons and hydroxyls at the interfaces.

We explore the local hydrogen-oxygen environments in terms of the 1st near-neighbor (NN) and 2nd NN hydrogen-oxygen distances (Fig. 6). The 1st and 2nd near-neighbors correspond, respectively, to intramolecular (direct oxygen-hydrogen bonds) and intermolecular hydrogen-bonding similar to that in the bulk water. The calculated average H-O distances of the 1st and 2nd NN vary considerably among different hydrous grain boundaries and remain within 2-5% of the corresponding distances in the bulk water. The 1st and 2nd NN H-O distances increase and decrease, respectively, with increasing pressure. The predicted increases in the average (direct) O-H bond distances for different hydrous grain boundaries remain within 2% over the pressure range 0 to 15 GPa, but the pressure-induced decreases in the 2nd NN distances are large (up to 11%), implying increased intermolecular hydrogen bonding with compression. The corresponding variations for the bulk water are about 1 and 10%, respectively. We note here that unlike 100% molecular H₂O species in the bulk water, the predominant species in the hydrous grain boundary interface is hydroxyl (Table I). Large differences are expected in medium and even short-order atomic arrangements between the grain boundary hydrous components and the bulk water. It is worth noting that the 2nd NN hydrogen-oxygen bonds at the grain boundary interfaces closely resemble the intermolecular bonding in water.

Hydration volume and enthalpy of the grain boundary

The dominance of hydroxyls and negligible interconnected molecular H₂O units at the grain boundary

interface imply dissociative adsorption of water to the grain boundaries. This causes a significant difference in the volume of the interfacial water and the pure bulk water. At low pressures, the bulk water has a larger volume than interfacial water. As a consequence, all hydrous grain boundaries display negative excess volume relative to their dry counterparts (Fig. 7a). This indicates a volume collapse associated with the hydration of the interface. While the volume difference is systematically suppressed with compression, it persists at all pressures. A negative volume of mixing has been reported for organic mixtures including aqueous solutions (Pal and Bhardwaj, 2002; Stec et al., 2014). A similar mixing behavior has been predicted for silicate melt-water solutions (Bajgain et al., 2015, Karki et al., 2020). Even in alloys, it has been argued that a large negative volume of mixing is essential for crystal-to-amorphous phase transformation (Kusunoki, 1993). Although the hydrous grain boundary system as a whole may not be considered as a melt solution, the adsorption of the hydrous component results in very different chemical surroundings (than the pristine phase) at the grain boundary interface and renders the interface to behave more like an amorphous phase.

The predicted initial non-linear change in the hydration volume with pressure for all hydrous grain boundaries (Fig. 7a) can be explained by the difference in the pressure-volume profiles of the hydrous grain boundaries and bulk water. The hydrous component at the grain boundary interfaces can be considered as a minor component with respect to the Mg_2SiO_4 content. This means that while hydrous contributions are non-negligible, Mg_2SiO_4 remains the major contributor to the physical properties of hydrous grain boundaries. From 0 to 5 GPa, the pressure-volume profiles for hydrous grain boundaries display a weak linear behavior with volume reductions of 4 – 5%, which are similar to their corresponding dry counterparts. On the other hand, for highly compressible bulk water a sharp non-linear decrease results in more than 30% reduction in volume within 5 GPa (Fig. S4). As a consequence, the hydration volumes show a rapid non-linear increase at the initial stages of the compression and a sluggish behavior thereafter.

Based on our results, most of the hydrous grain boundaries modeled here are stable relative to their dry counterparts at 0 GPa and all of them become increasingly stable at compressed conditions (Fig. 4 and 7b). This is consistent with the general notion that the hydrous component tends to stabilize the surfaces and interfaces (McHale et al., 1997; de Leeuw et al., 2000a, 2000b; Ushakov and Navrotsky, 2005; Chen and Navrotsky, 2010). For example, calorimetric experiments suggest that hydrous Mg_2SiO_4 surfaces are relatively more stable than anhydrous ones by about 1 J/m^2 (Chen and Navrotsky, 2010). To quantitatively assess the relative stability of the hydrous grain boundaries, we evaluate the hydration enthalpy as $\Delta H_{\text{hyd}} = (H_{\text{hyGB}} - H_{\text{GB}} - H_{\text{H}_2\text{O}})$, which is similar to the grain boundary formation enthalpy with respect to the dry grain boundary. The hydration energies calculated for hydrous grain boundaries in forsterite using empirical potentials (de Leeuw et al., 2000a) ranges from -180 to 50 kJ/mol at zero pressure. In comparison, our calculated hydration energy varies between -50 and 30 kJ/mol considering both the planar and stepped configurations of (011)/[100] type (Fig. 7b). Our results also show that the hydration enthalpy systematically decreases with compression and becomes negative for all of the grain boundaries at pressures above 5 GPa (Fig. 7b). Interestingly, all of the stepped boundaries display lower hydration enthalpies than their planar counterparts, implying even greater stability for the stepped boundaries. The magnitude of excess volume in all hydrous grain boundaries relative to the dry grain boundaries decreases rapidly initially and then gradually with increasing pressure. The negative excess volume at all pressures means that the hydrous component facilitates the compaction of the interfacial region which in turn increases the relative stability of hydrous grain boundaries on compression. The main driving factor for the predicted negative hydration enthalpy and negative excess volume may be the dissociated incorporation of water within the grain boundaries. This is consistent with the dissociated adsorption of water molecules at some oxide surfaces (Łodziana et al., 2004; Chen and Navrotsky, 2010; Zhao et al., 2016; Heiden et al., 2018).

Finally, we assess the energetics of the incorporation of the H₂O component in the bulk part and at the interface. The incorporation (hydration) enthalpy, calculated by substituting two Mg atoms, each with two H atoms and one Si atom with four H atoms (total 4H₂O) in the bulk region of planar 30.4° tilt grain boundary -bearing supercell always remains positive, though it systematically decreases with pressure (Fig 7b). On contrary, the hydration enthalpy for four H₂O units incorporated at the grain boundary remains negative at all pressures beyond 1 GPa (Fig. 7b). It is clear that the hydration enthalpy for the fully (16H₂O at the grain boundary) hydrated 30.4° tilt remains lower than that of the partially (4H₂O at the grain boundary) hydrated one. This implies some sort of dependence of the hydration enthalpy on the amount of hydrous component at the grain boundary. The calculated excess volume is negative and relatively large (-7 and -10 Å³ per H₂O for H₂O at the bulk and grain boundary incorporation, respectively) at zero pressure and it becomes less negative approaching zero as pressure increases (the corresponding values are -0.7 and -0.5 Å³ per H₂O at 15 GPa). Our results thus show that the hydration enthalpy of grain boundaries is mostly negative whereas the bulk incorporation enthalpy of H₂O remains positive. This also means that the hydrous components in Mg₂SiO₄ are likely to segregate to the grain boundary region, which is consistent with the general trend that grain boundaries in materials serve as sinks for impurity defects (Hiraga et al., 2003, 2004; Karki et al., 2015). A definitive answer, however, can only be obtained through a rigorous thermodynamic approach which is beyond the scope of the present study.

IMPLICATIONS

Hydrous grain boundaries in Mg₂SiO₄ forsterite for different configurations and orientations were simulated as a function of pressure up to 15 GPa using generalized gradient approximation and projector augmented wave method. Our first-principles results suggest that hydrous grain boundaries are stable and display negative excess volumes relative to their dry counterparts. The hydration

enthalpy of all grain boundaries considered becomes negative at pressures above 3 GPa. On the other hand, the enthalpy of H₂O incorporation in the bulk region remains positive at all pressures, thus suggesting that hydrous components are preferably segregated to the grain boundary region. The speciation of the hydrous component consists of hydroxyls and molecular H₂O species with a prevalence of the former at all pressures. The OH species shares oxygen with either both Mg and Si or only Mg, but the H₂O species gets adsorbed exclusively at Mg sites. Our structural analysis also indicates the presence of cation-anion coordination defects (e.g., five oxygen coordinated Mg) and significantly distorted polyhedra in the grain boundary regions. These structural features appear to resemble those of amorphous phases, such as hydrous silicate melt (Bajgain et al., 2015). Our comparisons among different grain boundaries imply that grain boundary orientations have less significance in terms of grain boundary stability and excess volume and as such, most grain boundaries behave similarly when they get hydrated. The calculated properties of the hydrous grain boundaries are relatively insensitive to the choice of the exchange-correlation functional (GGA versus LDA).

It is known that water is present in the mantle and plays an important role in the dynamics of the upper mantle (Ohtani, 2020). If water is dominated within the grain boundaries (but not in bulk crystals) as implied by our finding that hydrated grain boundaries are energetically favorable at elevated pressures, the role of water in the upper mantle materials may be significantly different. The effects on materials properties are likely to be different between hydrous bulk impurity defects and hydrous interfacial defects. Such changes in the properties may dramatically influence the mantle dynamics. For instance, grain boundaries are considered to facilitate fracture and plastic deformation (Duffy, 1986; Sutton and Balluffi, 1995) and provide faster pathways for ionic diffusion (Van Orman et al., 2003; Hayden and Watson, 2007, 2008; Dohmen, 2008). Moreover, because of their structural similarities, grain boundary regions may behave more like melt at elevated temperatures (Marquardt and Faul, 2018). Incorporation of water in the grain boundaries, which is energetically favorable at the crust and upper

mantle pressure, is expected to increase the dynamics of ionic diffusion, enhance the plastic deformation and decrease the mechanic fracture of the materials. The present study is expected to stimulate more studies on how hydration and grain boundaries play a role in the properties of different mantle materials using computational and experimental techniques.

ACKNOWLEDGMENTS

This work was supported as part of the Center for Performance and Design of Nuclear Waste Forms and Containers, an Energy Frontier Research Center funded by the U.S. Department of Energy, Office of Science, Basic Energy Sciences, under Award DE-SC0016584 and also by National Science Foundation (EAR 1014514 and EAR 1764140). The computational resources of the National Energy Research Scientific Computing Center, a DOE Office of Science User Facility supported by the Office of Science of the U.S. Department of Energy under Contract No. DE-AC02-05CH11231 and Louisiana State University (<http://www.hpc.lsu.edu>) were used.

REFERENCES CITED

- Adjaoud, O., Marquardt, K., Jahn, S. (2012) Atomic structures and energies of grain boundaries in Mg_2SiO_4 forsterite from atomistic modeling. *Physics and Chemistry of Minerals*, 39, 749–760.
- Asimow, P., Langmuir, C. (2003) The importance of water to oceanic mantle melting regimes. *Nature*, 421, 815–820.
- Bajgain, S., Ghosh, D. B., and Karki, B. B. (2015) Structure and density of basaltic melts at mantle conditions from first-principles simulations. *Nature Communications*, 6, 8578.
- Barr, C. M., Thomas, S., Hart, J. L., Harlow, W., Anber, E., and Taheri, M. L. (2018) Tracking the evolution of intergranular corrosion through twin-related domains in grain boundary networks. *npj Materials Degradation*, 2, 14.
- Carrier, B., Vandamme, M., Pellenq, R. J.-M., Bornert, M., Ferrage, E., Hubert, F., and Damme, H. V. (2016) Effect of Water on Elastic and Creep Properties of Self-Standing Clay Films. *Langmuir*, 32, 1370–1379.
- Chen, S., and Navrotsky, A. (2009) Calorimetric study of the surface energy of forsterite. *American Mineralogist*, 95, 112–117.
- Ceperley, D. M., Alder, B. J. (1980) Ground state of the electron gas by a stochastic method. *Physical Review Letters*, 45, 566–569.
- de Leeuw, N. H., Parker, S. C., Catlow, R. A., and Price, G. D. (2000a) Proton containing defects at forsterite {010} tilt grain boundaries and stepped surfaces. *American Mineralogist*, 85, 1143-1154.
- de Leeuw, N. H., Parker, S. C., Catlow, R. A., and Price, G. D. (2000b) Modelling the effect of water on the surface structure and stability of forsterite. *Physics and Chemistry of Minerals*, 27, 332–341.

- Dohmen, R., and Milke, R. (2010) Diffusion in polycrystalline materials: Grain boundaries, mathematical models, and experimental data. In J. J. Rosso, Ed., Diffusion in Minerals and Melts, 72, p. 921–970. Reviews in Mineralogy and Geochemistry, Mineralogical Society of America, Chantilly, Virginia.
- Dohmen, R. (2008) A new experimental thin film approach to study mobility and partitioning of elements in grain boundaries: Fe–Mg between olivines mediated by transport through an inert grain boundary. American Mineralogist, 93, 863–874.
- Duffy, D. M. (1986) Grain boundaries in ionic crystals. Journal of Physics C: Solid State Physics, 19, 4393–4412.
- Geisler, T., Dohmen, L., Lenting, C., and Fritzsche M. B. K. (2019) Real-time in situ observations of reaction and transport phenomena during silicate glass corrosion by fluid-cell Raman spectroscopy. Nature Materials, 18, 342 – 348.
- Ghosh, D. B., and Karki, B. B. (2014) First principles simulations of the stability and structure of grain boundaries in Mg₂SiO₄ forsterite. Physics and Chemistry of Minerals, 41, 163–171.
- Gillan, M. J., Alfe, D., and Michaelides, A., (2016) Perspective: How good is DFT for water? Journal of Chemical Physics, 144, 130901.
- Hayden, L. A., and Watson, E. B. (2007) A diffusion mechanism for core–mantle interaction. Nature, 450, 709–712.
- Hayden, L. A., and Watson, E. B. (2008) Grain boundary mobility of carbon in Earth's mantle: a possible carbon flux from the core. Proceedings of the National Academy of Sciences, USA, 105, 8537–8541.
- Heiden, S., Yue, Y., Kirsch, H., Wirth, J., Saalfrank, P., and Campen, R. K. (2018) Water dissociative adsorption on α -Al₂O₃ (1120) is controlled by surface site undercoordination, density, and

topology. *Journal of Physical Chemistry C*, 122, 6573–6584.

Henderson, M. A. (2002) The interaction of water with solid surfaces: fundamental aspects revisited. *Surface Science Reports*, 46, 1–308.

Hiraga, T., Anderson, I. M., and Kohlstedt, D. L. (2003) Chemistry of grain boundaries in mantle rocks, *American Mineralogist*, 88, 1015–1019.

Hiraga, T., Anderson, I. M., and Kohlstedt, D. L. (2004) Grain boundaries as reservoirs of incompatible elements in the Earth's mantle. *Nature*, 427, 699–703.

Hirth, G., and Kohlstedt, D. L. (1995) Experimental constraints on the dynamics of the partially molten upper mantle: Deformation in the diffusion creep regime. *Journal of Geophysical Research: Solid Earth*, 100, 1981–2001.

Jacobsen, S. D., Jiang, F., Mao, Z., Duffy, T. S., Smyth, J. R., Holl, C. M., and Frost, D. J. (2008) Effects of hydration on the elastic properties of olivine. *Geophysical Research Letters*, L14303, doi:10.1029/2008GL034398.

Karki, B. B., Ghosh, D. B., and Verma, A. K. (2015) First-principles prediction of pressure-enhanced segregation and migration at MgO grain boundaries. *American Mineralogist*, 100, 1053–1058.

Karki, B. B., Ghosh, D. B., and Banjara, D. (2020) Mixed incorporation of carbon and hydrogen in silicate melts under varying pressure and redox conditions. *Earth and Planetary Science Letters*, 549, 116520.

Karato, S.-I. (1990) The role of hydrogen diffusivity in the electrical conductivity of the upper mantle. *Nature*, 347, 272–273.

Karato, S.-I., and Wu, P. (1993) Rheology of the upper mantle: A synthesis. *Science*, 260, 771–778.

King, H. E., Stimpfl, M., Deymier, P., Drake, M. J., Catlow, C. R. A., Putnis, A., and de Leeuw, N. H.

(2010) Computer simulations of water interactions with low-coordinated forsterite surfacesites: Implications for the origin of water in the inner solar system. *Earth and Planetary Science Letters*, 300, 11–18.

Kohn, S. C. (1996) Solubility of H₂O in nominally anhydrous mantle minerals using 1H MAS NMR. *American Mineralogist*, 81, 1523–1526.

Kresse, G., and Furthmüller, J. (1996) Efficiency of ab-initio total energy calculations for metals and semiconductors using a plane-wave basis set. *Computational Materials Science*, 6, 15–50.

Kresse, G., and Joubert, D. (1999) From ultrasoft pseudopotentials to the projector augmented-wave method. *Physical Review B*, 59, 1758–1775.

Kuru, Y., Wohlschlogel, M., Welzel, U., and Mittemeijer, E. J. (2009) Large excess volume in grain boundaries of stressed, nanocrystalline metallic thin films: its effect on grain-growth kinetics. *Applied Physics Letters*, 95, 163112.

Kusunoki, K. (1993) Molecular dynamics study of crystal to amorphous phase transformation. M. Doyoma, J. Kihara, M. Tanaka and R. Yamamoto, Eds., In *Computer Aided Innovation of New Materials II*, p. 1463–1468. Elsevier Science Publishers B. V.

Liu, T., Gautam, S., Wang, H-W., Anovitz, L. M., Mamontov, E., Allard, L. F., and Cole, D. R. (2018) Structure and dynamics of water on the forsterite surface. *Physical Chemistry and Chemical Physics*, 20, 27822–27829.

Łodziana, Z., Topsøe, N. and Nørskov, J. (2004) A negative surface energy for alumina. *Nature Materials*, 3, 289–293.

Marquardt, K. and Faul, U. H. (2018) The structure and composition of olivine grain boundaries: 40 years of studies, status and current developments. *Physics and Chemistry of Minerals*. 45, 139–172.

- McHale, M. J., Auroux, A., Perrotta, A. J., and Navrotsky, A. (1997) Surface energies and thermodynamic phase stability in nanocrystalline aluminas. *Science*, 277, 788–791.
- Ohtani, E. (2020) The role of water in Earth's mantle. *National Science Review*, 7, 224–232.
- Pal, A., and Bhardwaj, R. K. (2002) Excess Molar Volumes and Viscosities for Binary Mixtures of 2-Propoxyethanol and of 2-Isopropoxyethanol with 2-Pyrrolidinone, *N*-Methyl-2-pyrrolidinone, *N,N*-Dimethylformamide, and *N,N*-Dimethylacetamide at 298.15 K. *Journal of Chemical and Engineering Data*, 47, 1128 – 1134.
- Perdew, J. P., Burke, K., and Ernzerhof, M. (1996) Generalized gradient approximation made simple. *Physical Review Letters*, 77, 3865.
- Pommier, A., Kohlstedt, D. L., Hansen, L. N., Mackwell, S., Tasaka, M., Heidelbach, F., and Leinenweber, K. (2018) Transport properties of olivine grain boundaries from electrical conductivity experiments. *Contributions to Mineralogy and Petrology*, 173, 41.
- Qian, X. R., and Chou, Y. T. (1982) Correlation between grain boundary corrosion and grain boundary energy in niobium bicrystals. *Philosophical Magazine A*, 45, 1075–1079.
- Suknev, S.V. (2019) Influence of Temperature and Water Content on Elastic Properties of Hard Rocks in Thaw/Freeze State Transition. *Journal of Mining Science*, 55, 185–193.
- Stec, M., Tatarczuk, A., Spiewak, D., and Wilk, A. (2014) Densities, Excess Molar Volumes, and Thermal Expansion Coefficients of Aqueous Aminoethylethanolamine Solutions at Temperatures from 283.15 to 343.15 K. *Journal of Solution Chemistry*, 43, 959–971.
- Stimpfl, A., Walker, A. M., Drake, M. J., de Leeuw, N. H., and Deymier, P. (2006) An ångström-sized window on the origin of water in the inner solar system: Atomistic simulation of adsorption of water on olivine. *Journal of Crystal Growth*, 294, 83–95.
- Sutton, A. P., and Balluffi, R. W. (1995) *Interfaces in crystalline materials*. Clarendon, Oxford.

- Ushakov, S. V. and Navrotsky, A. (2005) Direct measurements of water adsorption enthalpy on hafnia and zirconia. *Applied Physics Letters*, 87, 164103.
- Van Orman, J. A., Fei, Y., Hauri, E., and Wang, Y., (2003) Diffusion in MgO at high pressures: constraints on deformation mechanisms and chemical transport at the core–mantle boundary. *Geophysical Research Letters*, 30, doi:10.1029/2002GL016343.
- Verma, A. K., and Karki, B. B. (2010) First-principles simulations of MgO tilt grain boundary: structure and vacancy formation at high pressure. *American Mineralogist* 95, 1035–1041.
- Yang, W., Ji, S., Li, Z., and Wang, M. (2015) Grain boundary precipitation induced by grain crystallographic misorientations in an extruded Al–Mg–Si–Cu alloy. *Journal of Alloys and Compounds*, 624, 27–30.
- Ye, Y., Schwering, R. A., and Smyth, J. R. (2009) Effects of hydration on thermal expansion of forsterite, wadsleyite, and ringwoodite at ambient pressure. *American Mineralogist*, 94, 899–904.
- Zhao, W., Bajdich, M., Carey, S., Vojvodic, A., Nørskov, J. K., and Campbell, C. T. (2016) Water Dissociative Adsorption on NiO(111): Energetics and Structure of the Hydroxylated Surface. *ACS Catalysis*, 6, 11, 7377–7384.

TABLES

Table 1: Information about the simulated grain boundaries (grain boundaries) of two types, including grain boundary plane, tilt angle and configuration (planar P or stepped S) at zero pressure. For each case, the numbers of Mg₂SiO₄ units (N_B) and interfacial H₂O units (N_{H_2O}), the OH:H₂O ratio, hydrogen number density (ρ_H), and coordination proportions at the grain boundary are given. The numbers in the parentheses correspond to ~15 GPa.

Grain boundary type	(011)/[100]						(110)/[001]		
Grain boundary plane	(011)		(021)		(031)		(130)	(120)	(110)
Tilt angle	30.4° (P)	30.4° (S)	49.6° (P)	49.6° (S)	60.4° (P)	60.4° (S)	35.5° (S)	47.0° (S)	65.0° (S)
Bulk in f.u. (N_B)	52	104	68	60	92	108	100	108	72
H ₂ O in f.u. (N_{H_2O})	16	32	16	16	16	16	16	48	32
OH:H ₂ O	2.57 (2.57)	1.76 (1.76)	3.33 (4.4)	1.55 (1.55)	3.33 (2.57)	6.00 (4.40)	4.40 (4.40)	2.36 (1.69)	8.67 (7.14)
$\rho_H = 2x/A_{GB}$ (Å ⁻²)	0.281 (0.300)	0.281 (0.300)	0.212 (0.225)	0.211 (0.226)	0.161 (0.172)	0.161 (0.171)	0.147 (0.157)	0.276 (0.299)	0.228 (0.247)
3-fold O (%)	80 (64)	73 (60)	69 (59)	74 (65)	58 (40)	82 (68)	50 (33)	76 (63)	74 (59)
Si–O over (>4) coordination (%)	1.92 (1.92)	0.00 (0.96)	0.00 (0.00)	0.00 (0.00)	0.00 (0.00)	0.93 (0.93)	1.00 (3.00)	2.78 (4.63)	1.39 (4.17)
Mg–O under (<6) coordination (%)	3.84 (1.92)	3.84 (1.44)	5.15 (2.94)	10.0 (5.00)	8.69 (4.89)	10.2 (7.41)	21.0 (10.0)	20.8 (11.6)	20.8 (11.8)

Fig. 1: (a) Set of (011) planes in Mg_2SiO_4 supercells with angles (measured with the c -plane) 30.4° , 49.6° and 60.4° corresponding to the (011), (021) and (031) planes, respectively (left). With a as the axis of rotation, this set of grain boundaries is represented as (011)/[100]. (b) Modeling details for the unrelaxed anhydrous 49.6° tilt. To avoid the split edge view of the grain boundary at the supercell edges and provide better visual clarity, a slight rigid shift is given along the c direction. L_{GB} denotes the grain boundary unit length. (c) and (d) shows grain boundary regions for the unrelaxed 49.6° tilt before and after hydrogen substitution, respectively. Brown, blue, red and light green spheres denote Mg, Si, O and H atoms, respectively. Si's are also shown as cation-anion polyhedra. Note that the majority of Mg atoms in the interface is under-coordinated with respect to oxygen because grain boundary was created by Mg termination.

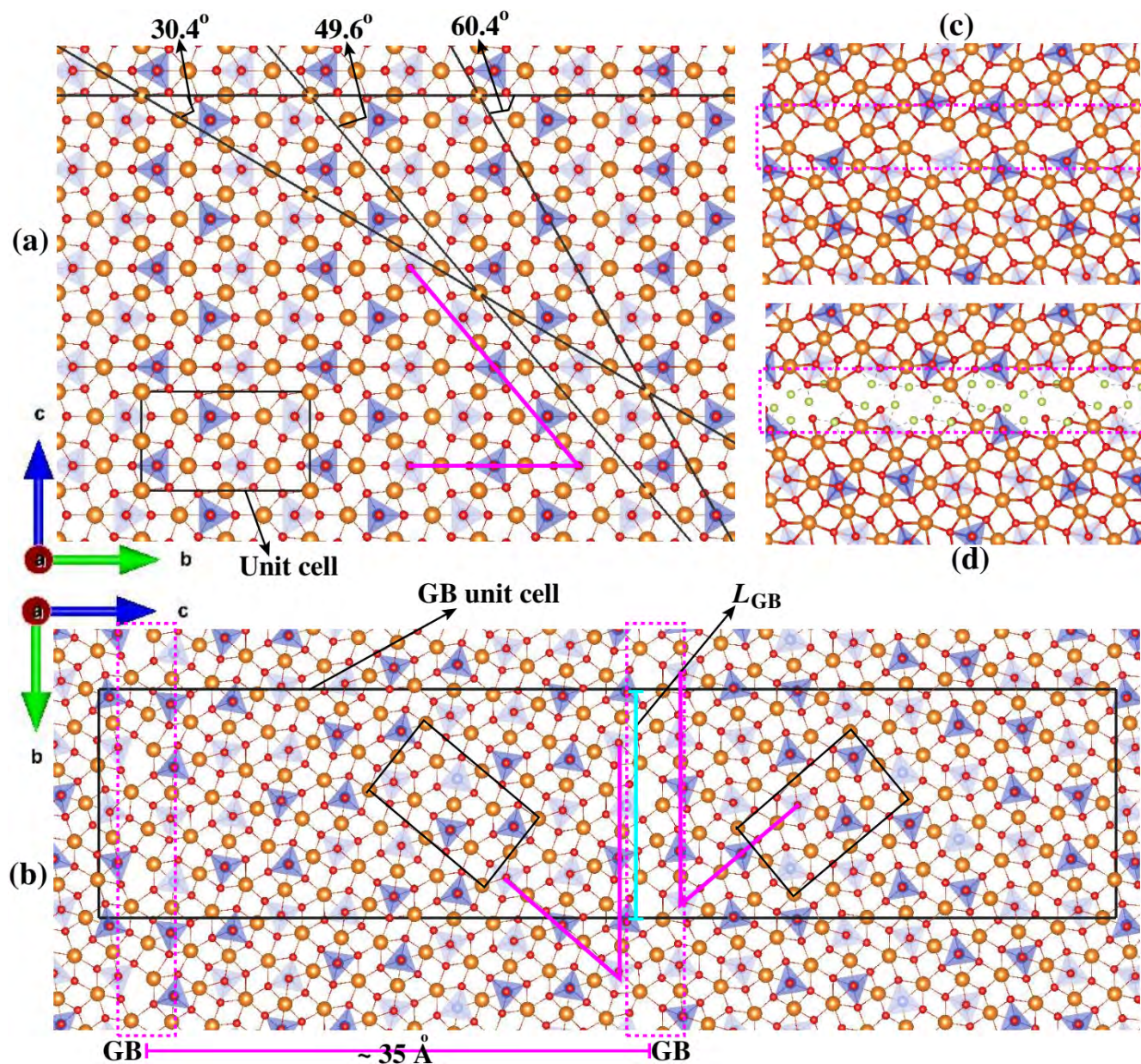


Fig. 2: Grain boundary structures for the 30.4° tilt in planar (left) and stepped (right) configurations, shown for unrelaxed (dry and hydrous), and relaxed hydrous grain boundaries at ~0 and ~15 GPa. Direct H-O (1st NN) bonds ($0 \leq \text{cutoff range} \leq 1.2 \text{ \AA}$) are represented as solid bi-color lines. The 2nd NN H-O bonds ($1.2 < \text{cutoff range} \leq 2.1 \text{ \AA}$) are represented by dashed gray lines. Atomic colors brown, blue, red and light green correspond to Mg, Si, O and H, respectively. Si's are also shown as cation-anion polyhedra. In the left panel grain boundary unit cells for the planar 30.4° configurations are marked as black rectangles. Right column figures show grain boundary unit cells for the stepped 30.4° tilt. Tilt angles are marked by magenta lines for anhydrous configurations. To avoid the split edge view of the grain boundary at the supercell edges and provide better visual clarity, a slight rigid shift along the *c* direction is given.

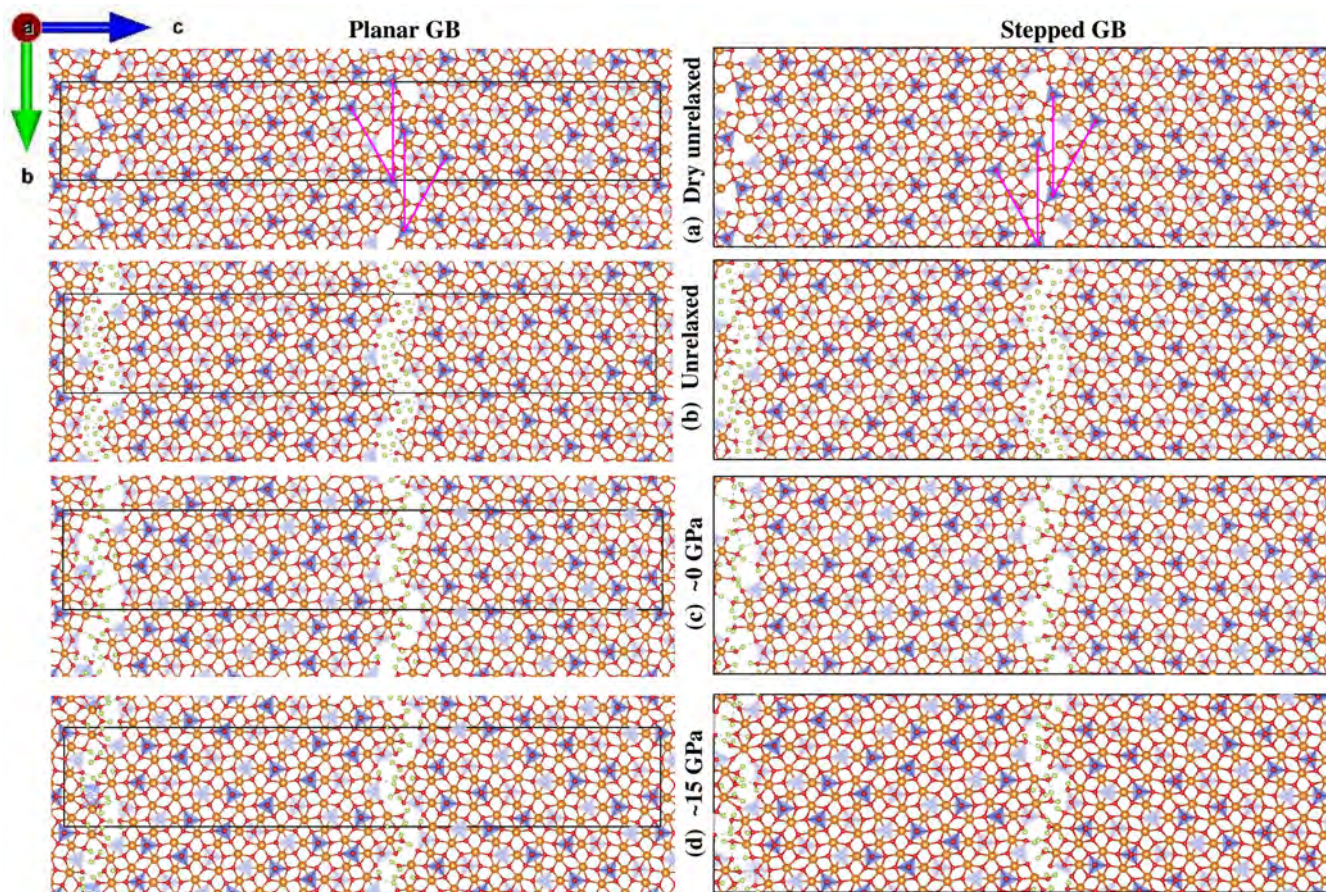


Fig. 3: Average Si-O and Mg-O bond length variation (right panel) and the corresponding distortion indices (left panel) along a distance perpendicular to the grain boundary plane for the 30.4° tilt angle shown at ~0 and ~15 GPa. Solid (red and blue) lines correspond to the calculated values for the crystalline Mg₂SiO₄. Red and blue symbols represent individual Mg or Si.

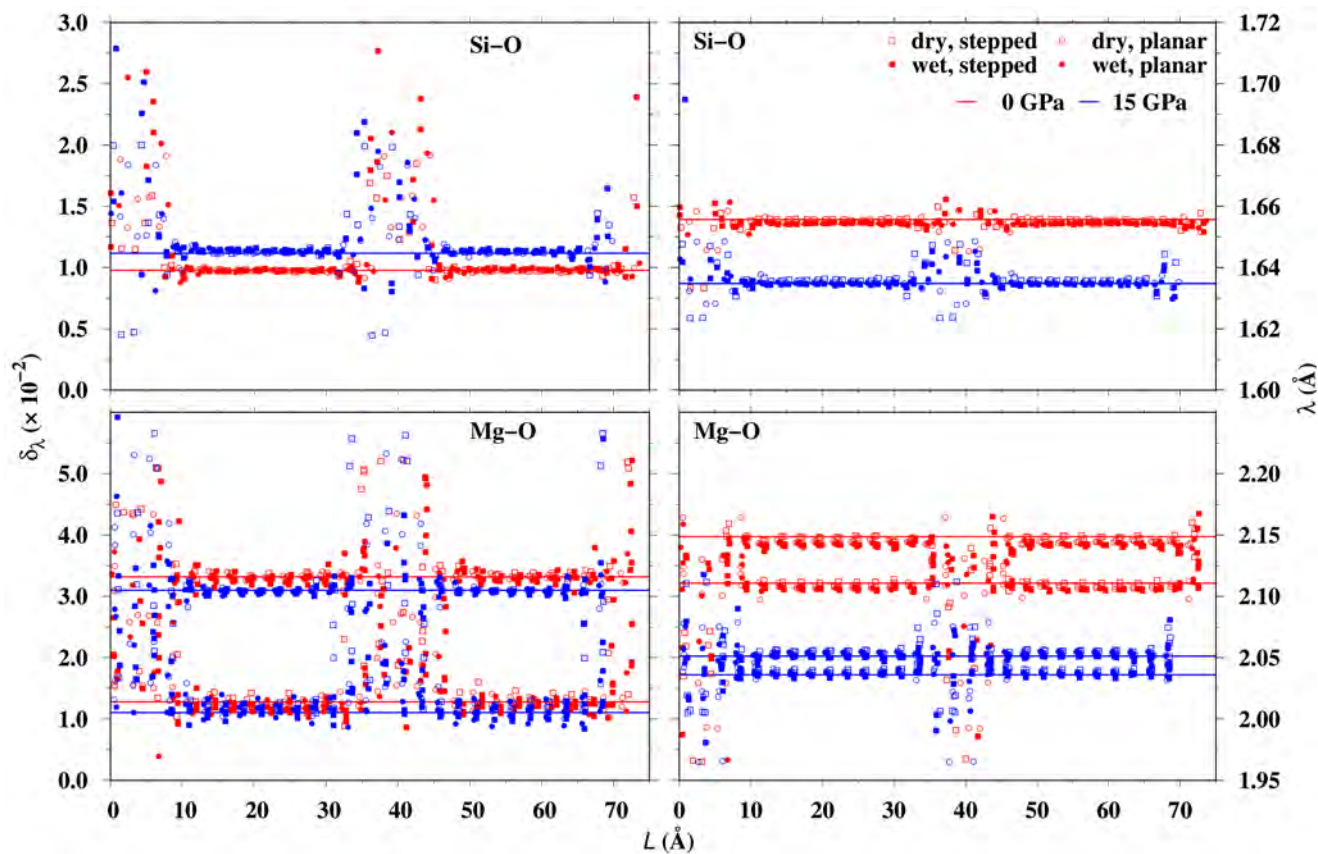


Fig. 4: Pressure variations of the calculated formation enthalpy of different (011)/[100] type grain boundaries in planar and stepped configurations (squares, circles and diamonds corresponding to tilt angles 30.4°, 49.6° and 60.4°, respectively). The open and solid symbols represent dry and wet (hydrous) grain boundaries, respectively. The results for hydrous stepped (110)/[001] configurations corresponding to tilt angles 35.5° and 47.0° and 65.0° are shown by asterisks, triangles and pluses, respectively. The LDA results for dry and wet planar grain boundaries (for 30.4° and 49.6° tilts) are shown by gray symbols.

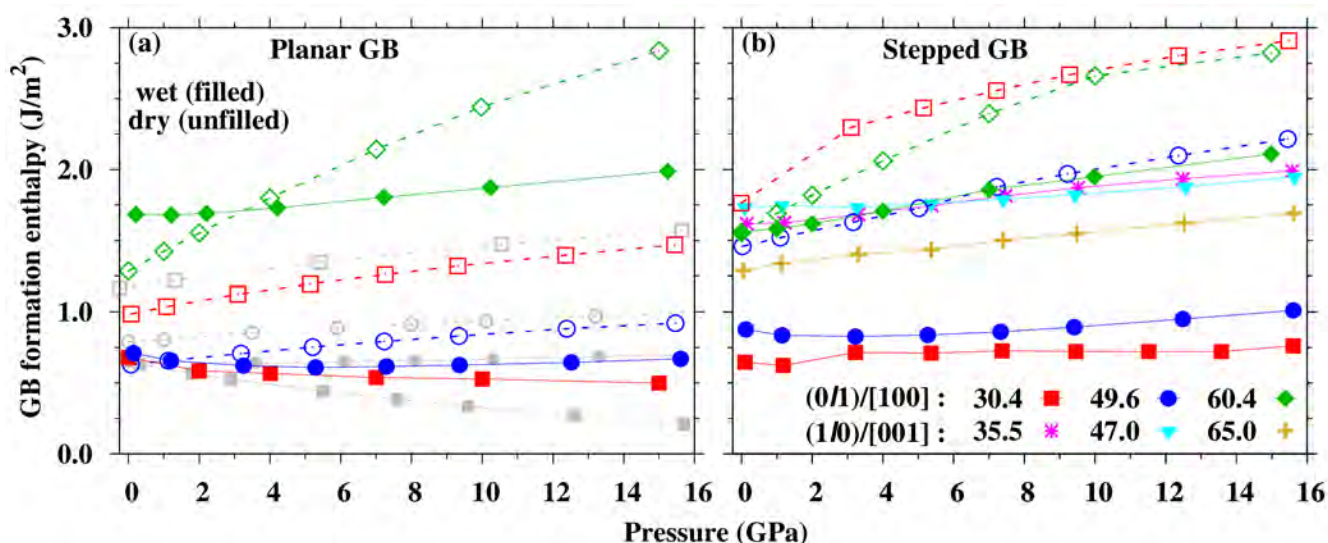


Fig. 5: Excess volume as a function of pressure for dry and wet (011)/[100] grain boundaries (squares, circles and diamonds corresponding to tilt angles 30.4° and 49.6° and 60.4°, respectively) and wet (110)/[001] grain boundaries (asterisks, triangles and pluses corresponding to tilt angles 35.5° and 47.0° and 65.0°). The LDA results for dry and wet planar grain boundaries (for 30.4° and 49.6° tilts) are shown by gray symbols.

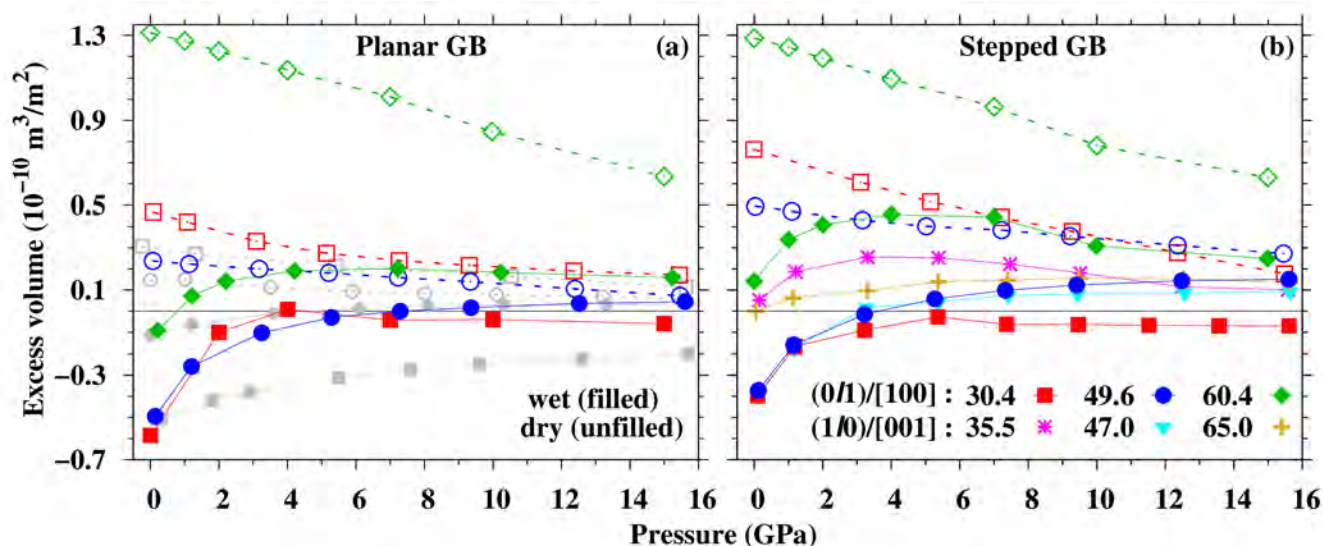


Fig. 6: Pressure variations of average H–O bond distances (a) and 2nd NN (nearest-neighbor) H–O distances (b) for planar and stepped (011)/[100] grain boundaries with tilt angles 30.4°, 49.6° and 60.4° (shown by squares, circles and diamonds, respectively). The corresponding H–O distances in the simulated bulk/pure water are shown for comparison (gray asterisks). A cutoff distance of 1.2 Å was used for H–O bonds and a window of 1.2–2.0 Å was used for 2nd NN.

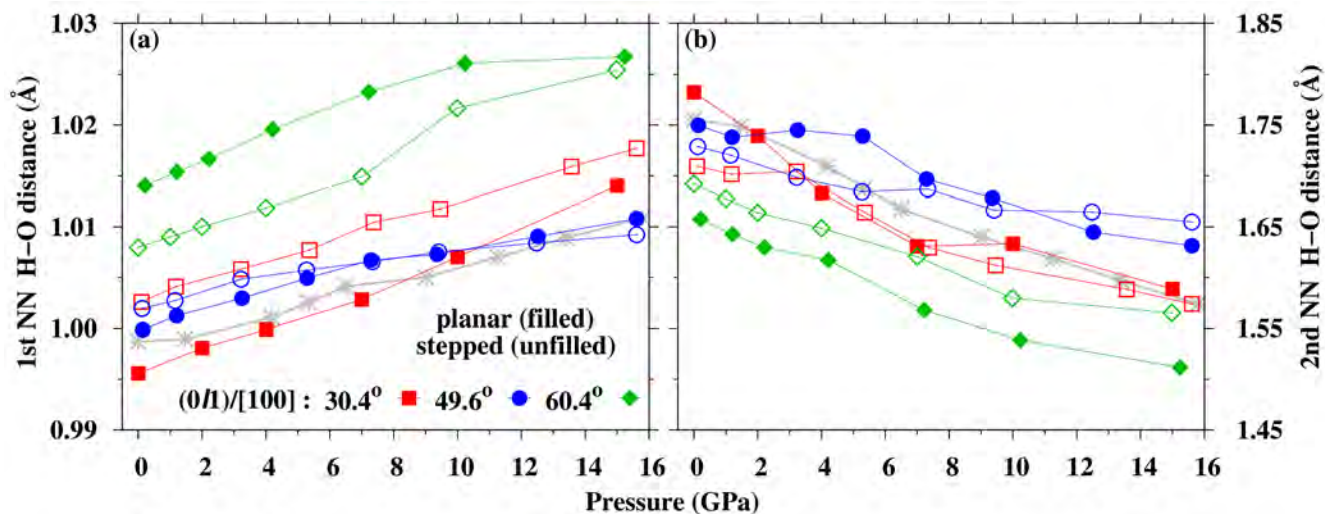


Fig. 7: Pressure variations of the hydration volume (a) and hydration enthalpy (b) with respect to the corresponding dry grain boundary configurations for planar and stepped (011)/[100] grain boundaries with tilt angles 30.4°, 49.6° and 60.4° (shown by squares, circles and diamonds, respectively). The LDA results for planar 30.4° and 49.6° tilt grain boundaries are shown in gray circles and squares, respectively. The hydration volume is scaled to per formula unit of H₂O. Also enthalpy results for the incorporation of H₂O in the bulk (black plus) and grain boundary (black asterisk) regions for the planar 30.4° tilt are shown for comparison.

